Article

Surfactant Engineering and Its Role in Determining the Performance of Nanoparticulate Organic Photovoltaic Devices

Riku Chowdhury, Natalie P. Holmes, Nathan Cooling, Warwick J. Belcher, Paul C. Dastoor,* and Xiaojing Zhou*

Cite This: ACS Omega 2022, 7, 9212−9220

Read Online

ACCESS | Metrics & More | Article Recommendations | Supporting Information

ABSTRACT: The fabrication of organic photovoltaics (OPVs) from non-hazardous nanoparticulate (NP) inks offers considerable promise for the development of eco-friendly large-scale printed solar modules. However, the typical NP core−shell morphology (driven by the different donor/acceptor affinities for the surfactant used in NP synthesis) currently hinders the photovoltaic performance. As such, surfactant engineering offers an elegant approach to synthesizing a more optimal intermixed NP morphology and hence an improved photovoltaic performance. In this work, the morphology of conventional sodium dodecyl sulfate (SDS) and 2-(3-thienyl) ethyloxybutylsulfonate (TEBS)-stabilized poly(3-hexylthiophene) (P3HT) donor:phenyl-C_{61}-butyric acid methyl ester ($PC_{61}BM$) acceptor NPs is probed using scanning transmission X-ray microscopy, UV−vis spectroscopy, grazing-incidence X-ray diffraction, and scanning electron microscopy. While the SDS-stabilized NPs exhibit a size-independent core−shell morphology, this work reveals that TEBS-stabilized NPs deliver an intermixed morphology, the extent of which depends on the particle size. Consequently, by optimizing the TEBS-stabilized NP size and distribution, NP-OPV devices with a power conversion efficiency that is ∼50% higher on average than that of the corresponding SDS-based NP-OPV devices are produced.
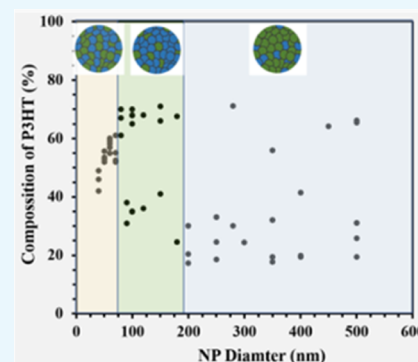
1. INTRODUCTION

It is widely recognized that renewable energy technologies will play a significant role in overcoming climate change, through reducing CO_2 emissions as well as natural resource consumption. Among the different sources of renewable energy, solar energy is a key contributor.[1] However, the conventional silicon-based solar cell technology still has limitations with respect to its energy/cost payback period and its long-term environmental impacts. Consequently, over the last few decades, researchers have focused on developing organic photovoltaic (OPV) technology, given that it is lightweight, flexible, recyclable, and can be manufactured on a large scale using low-cost solution-based printing processes.[2] Indeed, several life cycle cost analysis reports have confirmed that the OPV technology can contribute cost-effectively to the global energy supply.[1,2] Moreover, the current power conversion efficiency (PCE) of OPV at a laboratory scale is ∼18%,[3] which is comparable to those of mono- and polycrystalline-based silicon photovoltaics.

In recent years, the increase of the OPV device efficiency has been achieved through the design of new photoactive materials and improvements to the different buffer layers of the devices.[4] However, the challenge of large-scale fabrication is that OPV technology now has to meet a figure of merit (FOM) that combines both the PCE of the devices and the synthetic complexity (SC) of the materials.[5,6] From this perspective, the use of hazardous organic solvents is limited due to their potential for environmental pollution and harm to human health, resulting in higher SC and hence high fabrication costs. Consequently, researchers developing the industrialization of OPV technology have been actively working on alternative eco-friendly ("green") solvents.[7]

Nanoparticle (NP) ink technology (whereby donor and acceptor materials are processed to form nanoparticles using green solvents such as water or alcohols) enables both preaggregation of the donor/acceptor domains (resulting in beneficial phase separation akin to bulk heterojunction (BHJ) devices) and eco-friendly OPV fabrication.[8,9] In principle, there are two methodologies to prepare NPs: (a) precipitation and (b) miniemulsion. The first successful attempt to use the precipitation method for NP-OPV synthesis was reported by our group in 2011.[10] However, the precipitation method produces dispersions that are intrinsically unstable. This problem can be solved by the miniemulsion process, which is a common and powerful strategy for synthesizing stable
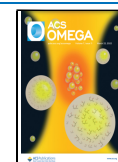
aqueous-processed nanoparticle inks.[9,11] Preparing stable aqueous NP dispersions of hydrophobic conjugated organic donor−acceptor materials is achieved by using surfactants, such as sodium dodecyl sulfate (SDS).[12]

The performance of SDS-processed NP-OPV devices is still limited, even for highly efficient donor−acceptor materials, due to several factors.[13] First, the presence of excess SDS surfactant inside the photoactive layer can form a dipole layer near the electrode interfaces due to the accumulation of the mobile surfactant. Consequently, charge extraction is limited and interfacial energy levels are altered, which lead to a poor device performance[14.] Although centrifugal dialysis is an effective strategy for removing excess surfactant from the dispersed NP inks, optimization is a complex process as overdialysis may lead to unstable suspensions and/or the formation of cavities due to changes in NP surface tension.[15] Second, the phase-separated core−shell nanostructure, which is typical in SDS-stabilized NPs,[16,17] results in poor exciton dissociation and hence reduced photo-current generation.[18] As such, the creation of a more highly intermixed donor/acceptor NP domain morphology is essential to enhance exciton dissociation and hence the NP-OPV performance.[19]

Recently, Subianto et al.[20] reported a structural study of P3HT/PC$_{61}$BM NPs synthesized using a thiophene-based surfactant, 2-(3-thienyl) ethyloxybutylsulfonate (TEBS), via the miniemulsion process. The UV−visible spectroscopy, contrast-variation small-angle neutron scattering (CV-SANS), and cyclic voltammetry (CV) results revealed a homogeneous distribution of small demixed donor and acceptor domains within the TEBS NP structure, which, as indicated by the authors, has the potential to improve film formation of a photoactive layer and consequently the NP-OPV performance. This work also highlighted the need for further studies of the detailed internal chemical composition and crystallinity of TEBS NPs, as well as analysis of the photovoltaic performance of TEBS NP-OPV devices.

In this paper, we have utilized a combination of scanning transmission X-ray microscopy (STXM), field-emission scanning electron microscopy (FESEM), X-ray diffraction (XRD), and UV−vis absorption spectroscopy to investigate the internal morphology of TEBS NPs in comparison with the performance of TEBS NP-OPV devices. In addition, the effect of TEBS NP and SDS NP size and distribution on the NP-OPV device performance is compared and contrasted. Consequently, a complete comparative study in terms of internal morphology of these new TEBS surfactant-stabilized aqueous NPs and the corresponding TEBS NP-OPV device performance over conventional SDS surfactant-based NPs and SDS NP-OPV devices is presented. In particular, this study explores the effect that changing internal NP morphology, through surfactant engineering, has on NP-OPV device efficiency.

2. DETAILS OF EXPERIMENTAL PROCEDURES

2.1. P3HT/PC$_{61}$BM NP Synthesis Procedure. Poly(3-hexylthiophene) (P3HT) (M_n 20 kDa) and PC$_{61}$BM were synthesized in house (Center for Organic Electronics, University of Newcastle, Australia) according to literature methods.[21,22] SDS (98% purity) and TEBS surfactants were purchased from Sigma-Aldrich and Solaris Chem, respectively. PEDOT:PSS (AI4083) as hole transport material was purchased from Heraeus, Germany and filtered through a 0.45 μm PVDF filter before use. To prepare an organic phase

(30 mg/mL) in the anhydrous chloroform solvent, 15 mg of P3HT polymer donor material and 15 mg of PC$_{61}$BM fullerene acceptor material were stirred at 500 rpm, 35 °C for 25 min on a hotplate. In parallel, an aqueous phase was prepared by mixing 20 mM of TEBS surfactant in 3 mL of filtered milli-Q water by stirring at 500 rpm for 25 min at room temperature. The combined organic and aqueous phases were then mixed by stirring at 1100 rpm and at 33 °C for 30 min to form a macroemulsion. A miniemulsion was then generated using a Hielscher UP400S (ultrahorn sonicator) at 70% amplitude for 3 min with a surrounding ice bath in place (to dissipate produced heat during sonication). The miniemulsion was transferred immediately onto a preset hotplate stirrer (1200 rpm, 60 °C, overnight) to evaporate the chloroform from the emulsion to form the solid nanoparticle dispersion. Finally, the dispersion was centrifuged (Hettich Zentrifugen Rotina 420) to remove excess surfactant as well as to concentrate the nanoparticle inks to an optimum solid loading of 10 wt % (overall TEBS NP synthesis process illustrated in Figure S1a). The SDS-processed P3HT/PC$_{61}$BM NPs were synthesized following the same protocol, as described elsewhere.[23]

2.2. Nanoparticle Characterization. Nanoparticle sizes were determined by scanning electron microscopy (SEM) and dynamic light scattering (DLS). For SEM analysis, both TEBS- and SDS-processed P3HT/PC$_{61}$BM nanoparticle dispersions (2.5 μL) were diluted with water (22.5 μL) in a ratio of 1:10 and then 5 μL of the diluted NP dispersions were spin-coated onto Si substrates at 3000 rpm, 112 rpm/s for 1 min. A Zeiss Sigma VP field emission scanning electron microscope was used with an acceleration voltage of 2−5 kV, an in-lens electron detector, and 5000−50,000 times magnification to record SEM images. A Malvern Instruments Zetasiser Nano-ZS ZEN3500 with a 633 nm laser and a backscatter detector angle of 173° was used for DLS nanoparticle size measurement. Samples for DLS were prepared by diluting 2.5 μL of the initial NP ink in 3 mL Milli-Q water.

Grazing-incidence X-ray diffraction analysis was performed on spin-coated films of the NP dispersion using a Phillips X'PertPRO MPD XRD, equipped with a Co Kα anode (λ = 1.78901 Å). The angle of incidence was fixed at ω = 0.5°, and data were collected for 2 h in the 2θ range from 3 to 50° in steps of 0.05°.

To measure the UV−vis spectrum, an ultraviolet−visible absorption spectrophotometer (Varian Cary 6000i) with an integrating sphere was used in the wavelength range of 200−1200 nm in a 1 nm step, with a deuterium plasma lamp for the 200−350 nm range and a tungsten halogen lamp for the 350−1200 nm range.

Samples were prepared for scanning transmission X-ray microscopy (STXM) by spin-coating a 2.5 μL nanoparticle dispersion at 3000 rpm, 1 min, and an acceleration of 112 rpm/s onto low-stress Si$_3$N$_4$ (silicon nitride) windows (0.25 × 0.25 mm^2, thickness of window was 15 nm, and the area of frame was 5 × 5 mm^2) with a silicon dioxide coating. Nanoparticles prepared for STXM morphological investigation had a higher concentration of organic phase (150 mg/mL) in the miniemulsion process with the aim of achieving both larger particles and a broader distribution in the particle size for imaging. These large nanoparticles had a diameter >500 nm as measured by DLS and SEM. As-cast (no thermal treatment) samples were air-dried. STXM measurements were performed at the Advanced Light Source on beamline 5.3.2.2[24] with the full method reported elsewhere.[23]
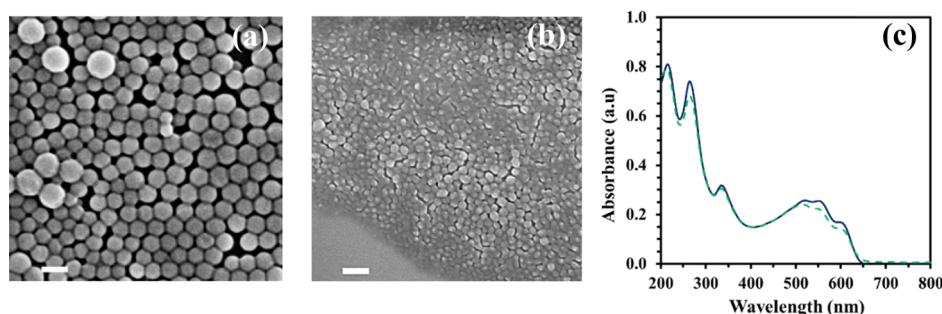
Figure 1. SEM images of (a) TEBS-P3HT/PC$_{61}$BM nanoparticles and (b) SDS-P3HT/PC$_{61}$BM nanoparticles. The scale bar in both SEM images is 100 nm. (c) UV–vis absorbance spectra of TEBS-P3HT/PC$_{61}$BM nanoparticle (green-dashed line) and SDS-P3HT/PC$_{61}$BM nanoparticle (blue solid line) spin cast thin films.
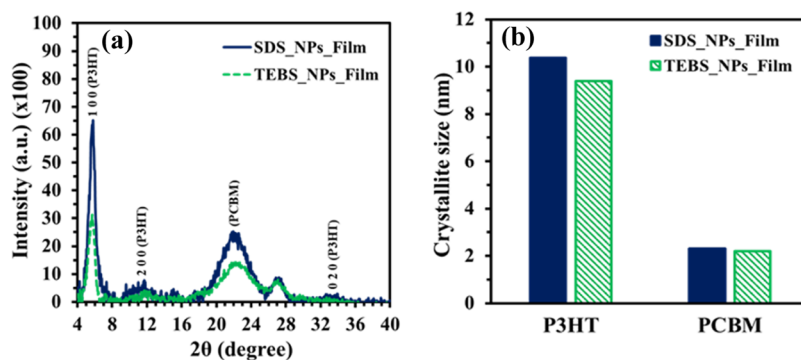
Figure 2. (a) XRD pattern of TEBS (green-dashed line)- and SDS (blue solid line)-processed P3HT/PC$_{61}$BM NP films on the glass substrate. (b) Estimated size of P3HT and PC$_{61}$BM crystallites from the width of the XRD peak, where green (diagonal stripes filled) and blue (solid filled) bars represent the crystalline domain size of TEBS- and SDS-processed NPs, respectively.

2.3. TEBS-Processed NP-Based NP-OPV Fabrication and Characterization. The NP-OPV devices were fabricated using SDS- and TEBS-processed NPs using a ITO/PEDOT:PSS/NP-P3HT/PC$_{61}$BM/ZnO/Al device structure. To fabricate the NP-OPV devices, precleaned (sequentially by water, acetone, and isopropanol for 10 min) patterned ITO substrates were treated by UV–ozone cleaning for 20 min. PEDOT:PSS (AI4083) films of 33 ± 6 nm thickness were spin-coated onto ITO at 5000 rpm (1 min) and then dried on a hotplate at 150 °C for 20 min. After that, the PEDOT:PSS-coated ITO substrates were treated for 10 min in a UV–ozone cleaner. SDS- or TEBS-processed P3HT/PC$_{61}$BM NP ink (35 μL) was spin-coated at 2000 and 1500 rpm, respectively, for 1 min and heated for 5 min at 110 °C to dry. The thickness of both surfactant-processed photoactive layers was optimized to 100 ± 10 nm. Subsequently, a ZnO film was deposited at 5000 rpm for 1 min and dried at 110 °C for 5 min in a nitrogen glove box. The thickness of the ZnO layer was measured with an average thickness of 15 ± 4 nm. Finally, 100 nm Al electrodes were deposited under vacuum conditions (10^{-6} Torr) via thermal evaporation using an Angstrom Amod deposition system.

The current density–voltage (J–V) measurements of fabricated NP-OPV devices were conducted using a Newport Class A solar simulator with an AM1.5 spectrum filter. The light intensity was measured to be 100 mW/cm^2 using a silicon reference solar cell (FHG-ISE), and the J–V data were recorded with a Keithley 2400 source meter. The NP-OPV devices were masked during testing under AM 1.5 conditions, where the masked area was 4 mm^2. External quantum efficiency (EQE) measurements were recorded by illuminating the OPV devices with a tungsten halogen lamp passed through an Oriel Cornerstone 130 monochromator. An Ithaco Dynatrac 395 analogue lock-in amplifier and a Thorlabs PDA55 silicon diode were employed to collect the reference signal, and a Stanford Research Systems SR830 DSP digitizing lock-in amplifier was employed to measure the device current.

3. RESULTS AND DISCUSSION

3.1. Characteristics and Internal Morphology of Stabilized P3HT/PC$_{61}$BM NPs. A SEM image of TEBS-stabilized P3HT/PC$_{61}$BM nanoparticles is presented in Figure 1a, which shows a mixture of semispherical-, spherical-, and hexagonal-shaped nanoparticles. By comparison, the conventional surfactant, SDS, and stabilized P3HT/PC$_{61}$BM nanoparticles were wrinkled and angular-shaped, as shown in Figure 1b, similar to those observed in our previous work.[20] The size distribution of the TEBS and SDS P3HT/PC$_{61}$BM NPS was measured by analyzing their corresponding SEM images using a circular Hough transform algorithm and is presented in Figure S1b. This analysis gave a mean particle diameter of 68 ± 13 and 28 ± 6 nm for TEBS- and SDS-stabilized P3HT/PC$_{61}$BM NPs, respectively. The size distributions were also measured using dynamic light scattering (DLS) for NP dispersions in water as shown in Figure S1c, where the size of the TEBS- and SDS-stabilized P3HT/PC$_{61}$BM NPs was measured to be 86.5 ± 11.7 and 46.7 ± 6.5 nm, respectively. The difference in the average TEBS and SDS NP size measured by the two techniques arises from the differences in the measurement environment. In the case of SEM, NPs were measured under dried conditions, whereas the DLS system measures the NP size in an aqueous dispersion and thus gives

the hydrodynamic size of the NPs. However, the size and distribution of TEBS-based NPs are consistently larger compared to those of SDS-based NPs for both SEM and DLS, in agreement with previous work.[20,25]

The NP shapes in the SEM images indicate a lower fraction of crystalline P3HT in the nanodomains of TEBS-stabilized P3HT/PC$_{61}$BM NPs relative to SDS-stabilized P3HT/PC$_{61}$BM NPs.[19] In order to further investigate the crystalline nature of both surfactant-processed NPs, UV−vis absorbance measurements were performed on spin-coated NP films as presented in Figure 1c. Spano and Clark et al.[26] have developed a relationship for the relative intensity of the polymer 0−0 transition (interchain) peak to the 0−1 transition (intrachain) peak, A_{0-0}/A_{0-1}, which is highly sensitive to the material microstructure, providing an indication of the degree of crystallinity. Hence, from the UV−vis spectrum, we measured the 0−0 transition peak at 610 nm and the 0−1 transition at 560 nm. In the case of SDS-stabilized P3HT/PC$_{61}$BM nanoparticles, the A_{0-0}/A_{0-1} ratio is 0.70, whereas the A_{0-0}/A_{0-1} ratio of TEBS-stabilized P3HT/PC$_{61}$BM nanoparticles is 0.6, indicating a lower fraction of crystalline P3HT in the TEBS-stabilized P3HT/PC$_{61}$BM NPs.

The observed lower crystallinity of TEBS-stabilized P3HT/PC$_{61}$BM NPs from the electron micrograph and UV−vis optical absorption data is also supported by the XRD spectra of the NP films as shown in Figure 2. The calculated crystalline P3HT domain size is 10.4 and 9.3 nm for the SDS- and TEBS-stabilized P3HT/PC$_{61}$BM NPs, respectively. Consequently, the SEM, UV−vis, and XRD measurements all confirm the presence of crystalline P3HT domains in both TEBS- and SDS-stabilized P3HT/PC$_{61}$BM NPs, while the XRD suggests a marginally smaller crystalline domain size, suggesting different internal structures.

In order to further investigate the internal morphology of the TEBS-stabilized P3HT/PC$_{61}$BM nanoparticles, STXM (which utilizes the chemical sensitivity of near edge X-ray absorption fine structure spectroscopy) was used to directly map the nanoscale structure. The STXM maps of the TEBS-stabilized P3HT/PC$_{61}$BM NPs are shown in Figure 3. Previous STXM measurement has revealed a PC$_{61}$BM-rich core and P3HT-rich shell morphology for SDS-stabilized P3HT/PC$_{61}$BM NPs.[16] The STXM fractional composition maps of P3HT in Figure 3a and PC$_{61}$BM in Figure 3b highlight that, whereas the internal morphology of the larger-sized (around 250 nm) TEBS-stabilized P3HT/PC$_{61}$BM nanoparticles is mostly dominated by PC$_{61}$BM (69 ± 11%), the smaller-sized (around 60 nm) TEBS NPs are more intermixed with P3HT and PC$_{61}$BM concentrations of 59 ± 5.8 and 45 ± 6.7%, respectively. The observed more intermixed chemical composition of sub 100 nm TEBS-stabilized NPs, as compared to SDS stabilized NPs, is consistent with the NP internal structure proposed by Subianto et al.,[20] where small demixed P3HT and PC$_{61}$BM domains were observed through neutron scattering and cyclic voltammetry analysis.

Surface energy is known to be a key driver of the NP internal morphology. In particular, the origin of the core−shell morphology typically observed in NP materials is determined mainly by the surface energy differential ($\Delta G_{surface} = G_{surface(acceptor)} - G_{surface(donor)}$) of the component materials, with the lower surface energy component segregating to the outermost surface during synthesis.[16,27−29] This conclusion is supported by the work of Kosco et al.,[25] who investigated the internal morphology of TEBS and SDS stabilized PTB7-Th
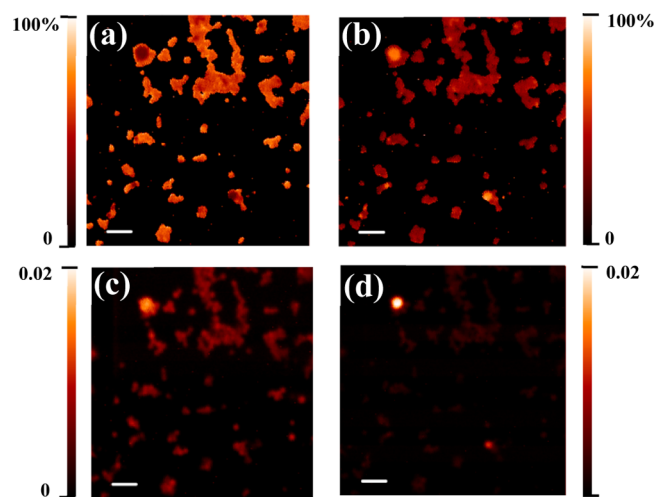
Figure 3. STXM fractional composition maps showing the concentration of (a) P3HT and (b) PC$_{61}$BM along with the corresponding STXM mass plots (c,d). All scale bars are 500 nm. The color contrast is scaled such that lighter colors relate to higher component concentrations. For the mass plots (c,d), the color scale bars present the concentration of components in mg/cm^2.

(polymer donor) and EH-IDTBR (non-fullerene acceptor) NPs using small-angle neutron scattering, cryo-TEM, and interfacial tension analyses. These studies revealed a more intimately mixed blend morphology for TEBS PTB7-Th/EH-IDTBR NPs as opposed to the core−shell morphology observed for SDS PTB7-Th/EH-IDTBR NPs. Surface tensiometer measurements showed that the chloroform/water interfacial tension in the presence of SDS was about double that observed when the chloroform phase contained EH-IDTBR (3.5 mN m^{-1}) compared to PTB7-Th (1.7 mN m^{-1}). This surface energy difference was attributed to the greater affinity between the long aliphatic tail of SDS and the higher alkyl chain density of the PTB7-Th donor compared with that of the EH-IDTBR acceptor. Because the affinity of SDS for PTB7-Th is higher than that of EH-IDTBR, radial phase segregation within the NP is thermodynamically favored, resulting in a PTB7-Th donor-rich shell and an EH-IDTBR acceptor-rich core morphology. By contrast, in the presence of TEBS, the chloroform/water interfacial tensions were almost identical, whether the chloroform phase contained EH-IDTBR (20.6 mN m^{-1}) or PTB7-Th (19.5 mN m^{-1}). In this case, relative to SDS, a surfactant with a shorter aromatic tail, such as TEBS,[20] will have increased affinity with the EH-IDTBR acceptor because it can interact more strongly with its exposed aromatic units. As the affinity of TEBS for PTB7-Th and EH-IDTBR is almost the same, radial phase segregation of PTB7-Th or EH-IDTBR within the NP is no longer thermodynamically favored, and the materials mix more homogeneously throughout the NP.

An analogous structural argument can be used to explain the changes in the morphology of NPs observed in the P3HT/PCBM donor/acceptor system. Because P3HT also has a considerably higher alkyl chain density than PCBM, a greater affinity between the SDS and P3HT will also be observed, leading to a similar core/shell morphology to that observed in PTB7-Th/EH-IDTBR NPs. By contrast, when TEBS is used as the surfactant, the smaller aromatic tail will allow for more balanced affinity between the TEBS and both P3HT and
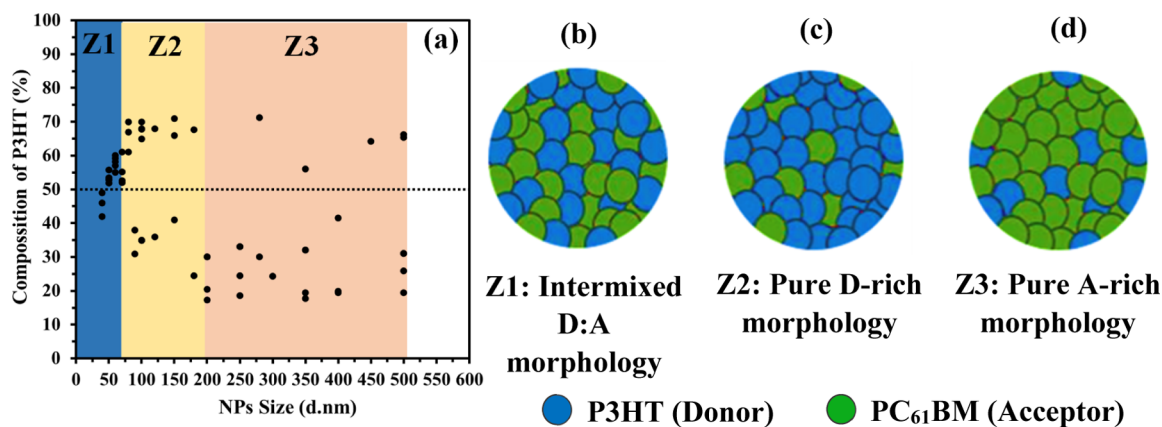
Figure 4. (a) Contribution of fractional composition mapping of the P3HT material in TEBS-processed P3HT/PC$_{61}$BM NPs, where the NP size is varied from 40 to 500 nm. The composition mapping (with standard deviation ranging from 6 to 12%) measured from composition maps of TEBS-processed P3HT/PC$_{61}$BM NPs STXM data as shown in Figure S3. The morphologies of (b) intermixed donor/acceptor, (c) pure donor-rich, and (d) pure acceptor-rich nanoparticles are drawn based upon the classified composition zones of Z1, Z2, and Z3, respectively, where the donor (P3HT) and acceptor (PC$_{61}$BM) materials are colored in blue and green, respectively.

PCBM, resulting in the observed more intermixed morphology.

3.2. Optimization of TEBS-Stabilized NP-Processed Photoactive Morphology. As discussed previously, the size and distribution of the TEBS P3HT/PC$_{61}$BM NPs is larger and broader than that of SDS P3HT/PC$_{61}$BM NPs, due to the lack of a well-defined critical micelle concentration (CMC) of the TEBS surfactant, resulting from the lower hydrophobicity of the thiophene group of TEBS compared to that of the alkyl chains in SDS.[20] In addition, the STXM fractional composition maps of P3HT and PC$_{61}$BM (Figure 3a,b) appear to depend on the size of the TEBS NPs. In order to quantify the role that the particle size plays in the internal morphology, STXM compositional mapping for a large set of TEBS P3HT/PC$_{61}$BM NPs (with sizes ranging from 40 to 500 nm) was undertaken and the variation of composition as a function of NP particle size, d, is plotted in Figure 4a. The data consist of three particle size regions: Z1, Z2, and Z3. In the Z1 region (40 nm < d < 70 nm), the NPs are more intermixed. In the Z2 region (75 nm < d < 200 nm), the chemical composition of the TEBS NPs appears to be mainly P3HT-rich with some PC$_{61}$BM-rich NPs present. In the Z3 region (d > 200 nm), the composition of the NPs is primarily PC$_{61}$BM-rich. This observation is summarized in the schematics of intermixed donor/acceptor, pure donor-rich, and pure acceptor-rich NP morphologies presented in Figure 4b−d, respectively. Importantly, the STXM data reveal that the TEBS P3HT/PC$_{61}$BM NPs tends toward a more phase-segregated internal morphology for larger-sized NPs (d > 80 nm).

NP morphology is determined by the relative affinities of the donor, acceptor, and surfactant materials. The high surface area to volume ratio of small micelles means that energetic terms associated with the surface dominate those associated with the bulk volume.[30] Thus, in the case of SDS (where the surfactant—donor and surfactant—acceptor affinities are significantly different), the higher affinity material is driven to the surface and ultimately a core—shell morphology ensues. By contrast, in the case of TEBS (where the surfactant—donor and surfactant—acceptor affinities are similar) neither donor nor acceptor material is driven to the micelle surface and a blended morphology occurs.

For larger micelles, the surface area to volume ratio is reduced, such that the energetic terms associated with the bulk volume now dominate. Thus, the dependence of NP composition with changing NP size is explained by the effect of the surfactant upon ripening of the initially formed liquid micelles. It is well established that the rate of ripening in a micellular system is highly dependent upon the surface modulus, or energy, of the surfactant used, with surfactants of higher surface modulus slowing the rate of ripening.[31] As such, micelles formed from TEBS, a low surface modulus surfactant, will have a rate of ripening that is much higher than those formed from SDS, resulting in larger micelles and consequently the observed larger particle size. As part of the ripening process, mass transport necessarily occurs between micelles via coalescence, compositional ripening, or Ostwald ripening.[32] If the initially intermixed materials within the micelle have a high affinity for each other (mutually miscible), then ripening leads to a change in the micelle size but not a change in composition.[32] However, if the materials are mutually immiscible (as is the case for P3HT and PCBM), then a change in composition occurs, driven by the self-affinity of the materials, resulting in the observed increase in material enrichment with increasing particle size.

The observation that the degree of intermixing of the donor and acceptor components decreases with increasing NP size is important and indicates that without any size control the TEBS P3HT/PC$_{61}$BM NP inks are unlikely to show any improvement in device efficiency over their SDS-based counterparts. Consequently, two approaches to create TEBS P3HT/PC$_{61}$BM NP inks with a narrower size distribution were adopted. First, the NP inks were allowed to age naturally, to see if the larger NPs would preferentially aggregate and fall out of solution. Second, the NP inks were centrifuged to rapidly remove the larger NPs directly from the solution.

The effect of aging on the TEBS NP size is shown in the left hand column of Figure 5, which shows representative SEM images of TEBS NPs deposited from the TEBS NP ink aged for 0, 30, 60, 90, and 180 days (Figure 5a−e) and the corresponding size distributions calculated from the SEM images (Figure 5f). Aging the inks for 60 days results in a systematic decrease in the average size of the TEBS NPs from 67 ± 14 to 53 ± 12 nm. In addition, the size distribution of the
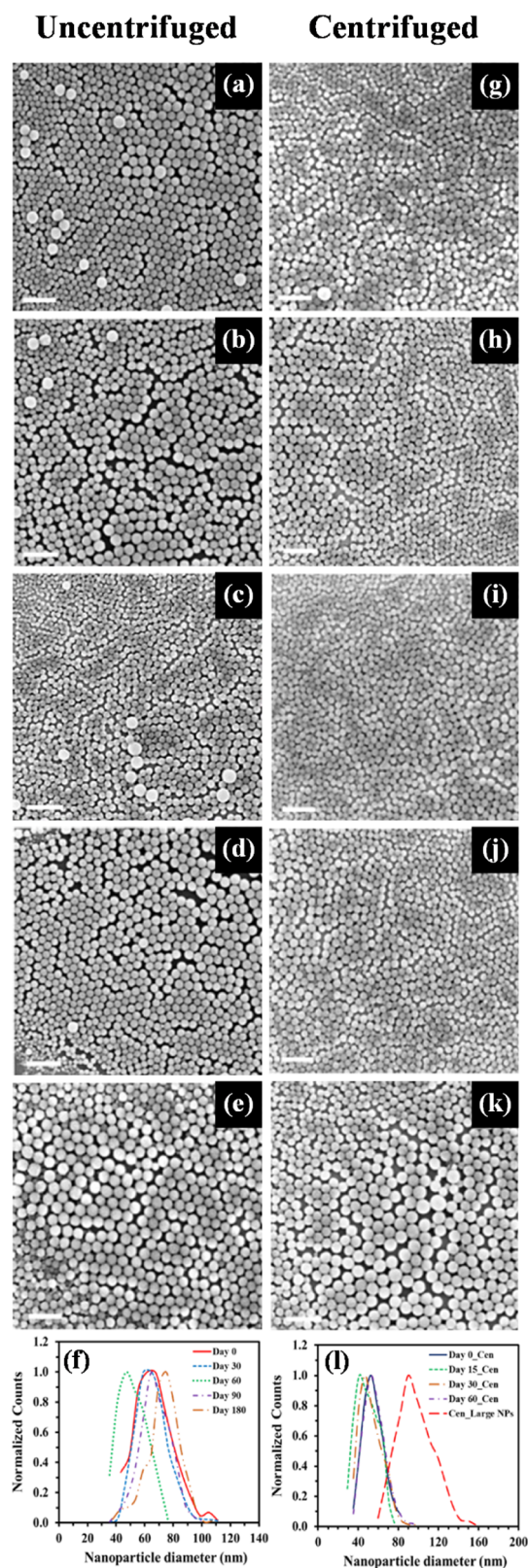
Figure 5. SEM images showing of uncentrifuged (a) day 0, (b) day 30, (c) day 60, (d) day 90, and (e) day 180 aged and centrifuged (g) day 0, (h) day 15, (i) day 30, (j) day 60, and (k) large TEBS-stabilized P3HT/PC$_{61}$BM nanoparticle size distribution, where the scale bars are 300 nm. The nanoparticle size distribution profiles of (f) uncentrifuged and (l) centrifuged TEBS inks are also shown.

TEBS NPs also became smaller and, significantly, the upper NP size limit was shifted below a threshold value of 80 nm, ensuring that the majority of NPs lay within the Z1 intermixed region identified by STXM. The reduction in the particle size arises from sedimentation of the larger NPs, which appears to progress through the first 60 days of aging. However, further aging of TEBS NPs results in an increase in the NP average size, which increases to 69 ± 10 nm after 90 day aging and then to 74 ± 12 nm after 180 day aging. The shift in the NP distribution profile toward larger-sized NPs with extended aging times is consistent with a slower aggregation of the smallest NPs in the ink solution.

The effect of centrifuging on the TEBS NP size is shown in the right hand column of Figure 5, which shows representative SEM images of the TEBS NPs aged for 0, 15, 30, and 60 days (Figure 5g−j) together with a SEM image of the large TEBS NPs removed from the ink by centrifuging (Figure 5k) and the corresponding size distributions calculated from the SEM images (Figure 5l). The average size of centrifuged fresh TEBS NPs (Figure 5g) dropped to 55 ± 10 nm compared to an uncentrifuged fresh TEBS NP size of 67 ± 14 nm (Figure 5a). The size and distribution of the NPs that were removed from the dispersion by centrifugation was also measured (Figure 5k) with an average size of 91 ± 17 nm and a maximum particle size of up to 160 nm (Figure 5l).

While centrifuging effectively removes NPs over 100 nm in size from the as-prepared TEBS NP dispersion, the distribution profile (Figure 5l) still exhibits a tail extending to NP sizes of 90 nm, indicating the presence of residual pure-phase NPs. As such, the centrifuged NPs were subsequently also aged to reduce the NP size and distribution. After 15 day aging, the average size of centrifuged NPs (Figure 5h) is slightly decreased to 49 ± 12 nm but the size distribution is reduced, now only extending to below 80 nm (Figure 5l). When the NPs are 30 and 60 day old, the average size of aged centrifuged TEBS NPs increased to 53 ± 13 nm (Figure 5i) and 57 ± 10 nm (Figure 5j), respectively, and the size distribution extends to preaging values (around 90 nm). Thus, it would appear that centrifuging the TEBS NPs, followed by 15 days of aging produces the optimal size and distribution of NPs for device preparation.

The device performance data for the uncentrifuged and centrifuged TEBS and SDS NP-OPV devices are summarized in Table 1, with more extensive device characteristics provided in the Supporting Information As expected, the performance of as-prepared TEBS NP-OPV devices is suboptimal, delivering hero (average ±standard deviation) unannealed and annealed efficiencies of 0.48% (0.46 ± 0.03%) and 0.82% (0.72 ± 0.08%), respectively. These values are lower than those of the corresponding SDS NP-OPV devices, which were 1.10% (0.86 ± 0.16%) and 1.24% (0.96 ± 0.20%) for unannealed and annealed devices, respectively. Upon aging for 60 days, the performance of TEBS NP-OPV improves considerably, increasing to 1.20% (1.03 ± 0.15%) and 1.51% (1.35 ± 0.10%) for unannealed and annealed devices, respectively. By contrast, the performance of as-prepared centrifuged TEBS NP-OPV devices is slightly lower than the 60-day aged centrifuged TEBS NP-OPV devices [0.87% (0.74 ± 0.10%) and 1.17% (0.95 ± 0.24%) for unannealed and annealed devices, respectively]. However, upon aging for 15 days, the performance of TEBS NP-OPV increases to 1.21% (1.01 ± 0.20%) and 1.55% (1.43 ± 0.14%) for unannealed and annealed devices, respectively. The performance data are

Table 1. Performance Comparison of w/ (Fresh and Best Aged Inks) and w/o (Fresh and Best Aged Inks) Centrifuged TEBS-Processed P3HT/PC$_{61}$BM Nanoparticle Inks with Respect to SDS-Stabilized P3HT/PC$_{61}$BM Nanoparticle Ink-Based NP-OPV Devices [Average ± Standard Deviation (Best)]

	aging NP ink-based NP-OPV		PCE (%)	V_{OC} (V)	FF (%)	J_{SC} (mA/cm^2)
			unannealed			
TEBS	W/O centrifuged	day 0	0.46 ± 0.03 (0.48)	0.33 ± 0.02 (0.32)	0.45 ± 0.01 (0.47)	3.07 ± 0.18 (3.21)
		day 60	1.03 ± 0.15 (1.2)	0.45 ± 0.01 (0.45)	0.44 ± 0.02 (0.47)	5.15 ± 0.69 (5.67)
	W/ centrifuged	day 0	0.74 ± 0.10 (0.87)	0.35 ± 0.02 (0.36)	0.42 ± 0.02 (0.47)	4.86 ± 0.50 (5.13)
		day 15	1.01 ± 0.20 (1.21)	0.42 ± 0.03 (0.46)	0.43 ± 0.06 (0.48)	5.37 ± 0.27 (5.50)
SDS		day 0	0.86 ± 0.16 (1.10)	0.40 ± 0.02 (0.43)	0.42 ± 0.04 (0.46)	5.03 ± 0.41 (5.59)
			annealed			
TEBS	W/O centrifuged	day 0	0.72 ± 0.08 (0.82)	0.32 ± 0.01 (0.34)	0.46 ± 0.03 (0.48)	4.84 ± 0.15 (5.02)
		day 60	1.35 ± 0.10 (1.51)	0.45 ± 0.02 (0.47)	0.48 ± 0.02 (0.50)	6.28 ± 0.10 (6.41)
	W/ centrifuged	day 0	0.95 ± 0.24 (1.17)	0.42 ± 0.03 (0.45)	0.45 ± 0.05 (0.48)	4.87 ± 0.50 (5.40)
		day 15	1.43 ± 0.14 (1.55)	0.46 ± 0.01 (0.45)	0.48 ± 0.02 (0.49)	6.39 ± 0.44 (7.02)
SDS		day 0	0.96 ± 0.20 (1.24)	0.42 ± 0.02 (0.43)	0.43 ± 0.03 (0.46)	5.30 ± 0.75 (6.25)
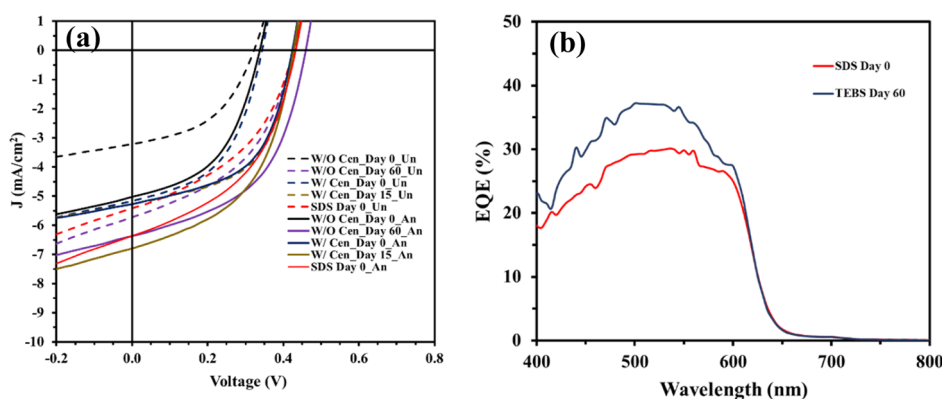
Figure 6. (a) $J-V$ characteristic curves of w/ (fresh and best aged inks) and w/o (fresh and best aged inks) centrifuged TEBS-processed P3HT/PC$_{61}$BM nanoparticle ink-based NP-OPV devices compared to SDS-based NP-OPV device performance. (b) EQE (%) of best uncentrifuged 60 day-aged TEBS NP ink and SDS fresh ink-based NP-OPV devices.

entirely consistent with the STXM data shown in Figure 4 and the morphology data shown in Figure 5, which predicted that the optimal NP morphology occurs for NPs lying within the Z1 region, which is achieved for NPs aged for 60 days or centrifuged and aged for 15 days. It should also be noted that our best NP-OPV devices with ZnO as the electron transfer layer (ETL) in this work show lower V_{OC} but higher J_{SC} than devices using Calcium as the ETL reported by Al-Mudhaffer et al.[18] and Ulum et al.[28]

The current density versus voltage ($J-V$) curves for the uncentrifuged and centrifuged TEBS and SDS NP-OPV devices are shown in Figure 6. For the unannealed devices, changing the particle size distribution of the TEBS-based NPs systematically affects the open-circuit voltage (V_{OC}) and short-circuit current density (J_{SC}), while the fill factor (FF) remains unchanged, consistent with both the NP morphology and film quality improving upon removal of the larger TEBS NPs (Supporting Information Figures S4 and S5). By contrast, for the annealed devices, the PCE improvement produced by reducing the particle size distribution is dominated by increased J_{SC}, indicating that: (i) more intermixed photoactive donor−acceptor morphologies are formed leading to enhanced charge dissociation and (ii) higher-quality thin photoactive layers are formed, which are beneficial for efficient charge transport. This observation is further borne out by the comparison of the external quantum efficiency (EQE) of the optimally aged TEBS and SDS NP-OPV devices as presented

in Figure 6b. The hero PCE of the optimal TEBS NP-OPV devices (with and without centrifugation) is almost the same (1.55 and 1.51%, respectively) and hence only the EQE of the optimally aged TEBS NP-OPV device was measured and compared with the EQE of the corresponding SDS-based device. Both the TEBS-based and SDS-based EQEs exhibit similar profiles as a function of incident photon wavelength, but the quantum yield for the TEBS-based NP device is much higher, consistent with a more optimal intermixed NP morphology. Indeed, the device performance of overaged TEBS NPs, whether (90 or 180 days) aged uncentrifuged inks or (30 or 60 days) aged centrifuged aged inks, decreases systematically [Supporting Information Table S1 (Figure S6) and Table S2 (Figure S7), respectively]. This observed decrease in performance is consistent with overaging resulting in larger NP sizes and thus pure donor (region Z2)- or acceptor (region Z3)-dominated NP morphologies (Figure 4) with correspondingly reduced charge dissociation.

From the overall chemical and optical studies on TEBS-processed aqueous NPs, it is observed that TEBS as a surfactant is not only able to form stable water-processed dispersed NP inks but also generates a well intermixed donor−acceptor NP morphology, in contrast to the core−shell NP morphology typical for SDS-processed aqueous NPs. Consequently, NP-OPV devices fabricated from optimized TEBS NP inks exhibit ~50% higher performance on average than those fabricated from SDS NP inks. The desired homogenous

intermixed donor—acceptor morphology has been achieved through the understanding that the nanomorphology is a function of particle size. Hence, through judicious control of the TEBS NP particle size distribution, it is possible to overcome the non-optimal core—shell distribution of donor and acceptor material domains typical of non-TEBS-based NPs.[33] As such, this work offers a pathway for developing a range of TEBS-based NPs from different donor—acceptor materials with controlled morphologies; thereby enhancing the performance of eco-friendly OPV devices to a competitive level with other OPV technologies.

4. CONCLUSIONS

In summary, eco-friendly photoactive nanoparticle inks were synthesized using TEBS as a surfactant, and the internal morphology and optical properties of the subsequent NPs were characterized using a combination of UV—vis spectroscopy, XRD, and STXM. The STXM maps of TEBS-processed P3HT/PC$_{61}$BM NPs revealed an intermixed donor/acceptor morphology that was particle size dependent, as opposed to the core—shell structure observed in SDS-based NPs of all sizes. This intermixed morphology is driven by surface energy, with TEBS having a similar affinity for both P3HT and PCBM. Consequently, optimization of the NP size and distribution boosted the performance of TEBS-based NP-OPV devices, resulting in a PCE enhancement of about 50% compared to conventional SDS-based NP-OPV devices. This work demonstrates that more intermixed internal NP morphologies lead to improved exciton dissociation and charge transport inside the photoactive layer, which ultimately increases the current density and overall device performance. The demonstration of controllable NP morphology using TEBS surfactants offers a new strategy toward the industrial production of OPVs from eco-friendly aqueous-processed NPs.

ASSOCIATED CONTENT

Supporting Information

The Supporting Information is available free of charge at https://pubs.acs.org/doi/10.1021/acsomega.1c05711.

> Optimized miniemulsion protocol for TEBS-stabilized P3HT/PC$_{61}$BM nanoparticle synthesis; measured TEBS- and SDS-stabilized P3HT/PC$_{61}$BM NP size distribution from the SEM images and the dispersed NPs in water using the DLS technique; spin-coated TEBS-stabilized NP films on glass substrates; STXM percentage composition maps of different sizes of TEBS NPs; comparison of the quality of TEBS-stabilized P3HT/PC$_{61}$BM nanoparticle films on glass from day 0, day 30, day 60, day 90, and day 180 aged inks; centrifuged TEBS-stabilized P3HT/PC$_{61}$BM nanoparticle films on glass substrates from day 0, day 15, day 30, and day 60 aged ink; comparison of performance of uncentrifuged fresh to different aged TEBS-stabilized P3HT/PC$_{61}$BM nanoparticle ink-based NP-OPV devices and SDS-based NP-OPV devices; comparison of the performance parameters of PCE (%), V_{OC}, J_{SC} (mA/cm^2), FF (%), and $J-V$ characteristic curves of TEBS-processed fresh to aged NP ink-based NP-OPV devices and those of SDS fresh ink-based NP-OPV devices; performance comparison of w/ (fresh and different aged inks) and w/o (fresh and based aged inks) centrifuged TEBS-processed P3HT/PC$_{61}$BM nanoparticle ink with

respect to SDS-stabilized P3HT/PC$_{61}$BM nanoparticle ink-based NP-OPV devices; and comparison of the performance parameters of PCE (%), V_{OC}, fill factor (%), J_{SC} (mA/cm^2), and $J-V$ characteristic curves of w/ (fresh and different aged inks) and w/o (fresh and based 60 day aged inks) centrifuged TEBS-processed P3HT/PC$_{61}$BM nanoparticle ink-based NP-OPV devices and those of the SDS-based NP-OPV devices (PDF)

AUTHOR INFORMATION

Corresponding Authors

Paul C. Dastoor − *Centre for Organic Electronics, College of Engineering, Science and Environment, The University of Newcastle, Callaghan, New South Wales 2308, Australia*; Email: paul.dastoor@newcastle.edu.au

Xiaojing Zhou − *Centre for Organic Electronics, College of Engineering, Science and Environment, The University of Newcastle, Callaghan, New South Wales 2308, Australia*; orcid.org/0000-0002-8912-598X; Email: xiaojing.zhou@newcastle.edu.au

Authors

Riku Chowdhury − *Centre for Organic Electronics, College of Engineering, Science and Environment, The University of Newcastle, Callaghan, New South Wales 2308, Australia*

Natalie P. Holmes − *Australian Centre for Microscopy and Microanalysis, University of Sydney, Sydney, New South Wales 2006, Australia*; orcid.org/0000-0002-8860-7098

Nathan Cooling − *Centre for Organic Electronics, College of Engineering, Science and Environment, The University of Newcastle, Callaghan, New South Wales 2308, Australia*

Warwick J. Belcher − *Centre for Organic Electronics, College of Engineering, Science and Environment, The University of Newcastle, Callaghan, New South Wales 2308, Australia*

Complete contact information is available at:
https://pubs.acs.org/10.1021/acsomega.1c05711

Notes

The authors declare no competing financial interest.

REFERENCES

(1) Pandey, A. K.; Tyagi, V. V.; Selvaraj, J. A. L.; Rahim, N. A.; Tyagi, S. K. Recent advances in solar photovoltaic systems for emerging trends and advanced applications. *Renew. Sustain. Energy Rev.* **2016**, 53, 859−884.

(2) Muteri, V.; Cellura, M.; Curto, D.; Franzitta, V.; Longo, S.; Mistretta, M.; Parisi, M. L. Review on life cycle assessment of solar photovoltaic panels. *Energies* **2020**, *13*, 252.

(3) Liu, Q.; Jiang, Y.; Jin, K.; Qin, J.; Xu, J.; Li, W.; Xiong, J.; Liu, J.; Xiao, Z.; Sun, K.; Yang, S.; Zhang, X.; Ding, L. 18% Efficiency organic solar cells. *Sci. Bull.* **2020**, *65*, 272−275.

(4) Rammal, M.; Lévêque, P.; Schlatter, G.; Leclerc, N.; Hébraud, A. Recent advances in the green processing of organic photovoltaic devices from nanoparticle dispersions. *Mater. Chem. Front.* **2020**, *4*, 2904−2931.

(5) Chochos, C. L.; Spanos, M.; Katsouras, A.; Tatsi, E.; Drakopoulou, S.; Gregoriou, V. G.; Avgeropoulos, A. Current status, challenges and future outlook of high performance polymer semiconductors for organic photovoltaics modules. *Prog. Polym. Sci.* **2019**, *91*, 51−79.

(6) Cooling, N. A.; Barnes, E. F.; Almyahi, F.; Feron, K.; Al-Mudhaffer, M. F.; Al-Ahmad, A.; Vaughan, B.; Andersen, T. R.; Griffith, M. J.; Hart, A. S.; Lyons, A. G.; Belcher, W. J.; Dastoor, P. C. A low-cost mixed fullerene acceptor blend for printed electronics. *J. Mater. Chem. A* **2016**, *4*, 10274−10281.

(7) Zhang, S.; Ye, L.; Zhang, H.; Hou, J. Green-solvent-processable organic solar cells. *Mater. Today* **2016**, *19*, 533−543.

(8) Gärtner, S.; Christmann, M.; Sankaran, S.; Röhm, H.; Prinz, E.-M.; Penth, F.; Pütz, A.; Türeli, A. E.; Penth, B.; Baumstümmler, B.; Colsmann, A. Eco-Friendly Fabrication of 4% Efficient Organic Solar Cells from Surfactant-Free P3HT:ICBA Nanoparticle Dispersions. *Adv. Mater.* **2014**, *26*, 6653−6657.

(9) Ghazy, O.; Freisinger, B.; Lieberwith, I.; Landfester, K. Tuning the size and morphology of P3HT/PCBM composite nanoparticles: towards optimized water-processable organic solar cells. *Nanoscale* **2020**, *12*, 22798−22807.

(10) Darwis, D.; Elkington, D.; Sesa, E.; Cooling, N.; Bryant, G.; Zhou, X.; Belcher, W.; Dastoor, P.; Dastoor, P.; Iskandar, F. Surfactant Free P3HT/PCBM Nanoparticles for Organic Photo-voltaics (OPV). *AIP Conf. Proc.* **2011**, *1415*, 120−123.

(11) Landfester, K. The generation of nanoparticles in mini-emulsions. *Adv. Mater.* **2001**, *13*, 765−768.

(12) Subianto, S.; Dutta, N.; Andersson, M.; Choudhury, N. R. Bulk heterojunction organic photovoltaics from water-processable nano-materials and their facile fabrication approaches. *Adv. Colloid Interface Sci.* **2016**, *235*, 56−69.

(13) D'Olieslaeger, L.; Pirotte, G.; Cardinaletti, I.; D'Haen, J.; Manca, J.; Vanderzande, D.; Maes, W.; Ethirajan, A. Eco-friendly fabrication of PBDTTPD:PC71BM solar cells reaching a PCE of 3.8% using water-based nanoparticle dispersions. *Org. Electron.* **2017**, *42*, 42−46.

(14) Ameri, M.; Al-Mudhaffer, M. F.; Almyahi, F.; Fardell, G. C.; Marks, M.; Al-Ahmad, A.; Fahy, A.; Andersen, T.; Elkington, D. C.; Feron, K.; Dickinson, M.; Samavat, F.; Dastoor, P. C.; Griffith, M. J. Role of Stabilizing Surfactants on Capacitance, Charge, and Ion Transport in Organic Nanoparticle-Based Electronic Devices. *ACS Appl. Mater. Interfaces* **2019**, *11*, 10074−10088.

(15) Almyahi, F.; Andersen, T. R.; Cooling, N. A.; Holmes, N. P.; Griffith, M. J.; Feron, K.; Zhou, X.; Belcher, W. J.; Dastoor, P. C. Optimisation of purification techniques for the preparation of large-volume aqueous solar nanoparticle inks for organic photovoltaics. *Beilstein J. Nanotechnol.* **2018**, *9*, 649−659.

(16) Holmes, N. P.; Burke, K. B.; Sista, P.; Barr, M.; Magurudeniya, H. D.; Stefan, M. C.; Kilcoyne, A. L. D.; Zhou, X.; Dastoor, P. C.; Belcher, W. J. Nano-domain behaviour in P3HT:PCBM nano-particles, relating material properties to morphological changes. *Sol. Energy Mater. Sol. Cells* **2013**, *117*, 437−445.

(17) Richards, J. J.; Whittle, C. L.; Shao, G.; Pozzo, L. D. Correlating structure and photocurrent for composite semiconducting nano-particles with contrast variation small-angle neutron scattering and photoconductive atomic force microscopy. *ACS Nano* **2014**, *8*, 4313−4324.

(18) Al-Mudhaffer, M. F.; Griffith, M. J.; Feron, K.; Nicolaidis, N. C.; Cooling, N. A.; Zhou, X.; Holdsworth, J.; Belcher, W. J.; Dastoor,

P. C. The origin of performance limitations in miniemulsion nanoparticulate organic photovoltaic devices. *Sol. Energy Mater. Sol. Cells* **2018**, *175*, 77−88.

(19) Marks, M.; Holmes, N. P.; Sharma, A.; Pan, X.; Chowdhury, R.; Barr, M. G.; Fenn, C.; Griffith, M. J.; Feron, K.; Kilcoyne, A. L. D.; Lewis, D. A.; Andersson, M. R.; Belcher, W. J.; Dastoor, P. C. Building intermixed donor-acceptor architectures for water-processable organic photovoltaics. *Phys. Chem. Chem. Phys.* **2019**, *21*, 5705−5715.

(20) Subianto, S.; Balu, R.; de Campo, L.; Sokolova, A.; Dutta, N. K.; Choudhury, N. R. Sulfonated Thiophene Derivative Stabilized Aqueous Poly(3-hexylthiophene):Phenyl-C61-butyric Acid Methyl Ester Nanoparticle Dispersion for Organic Solar Cell Applications. *ACS Appl. Mater. Interfaces* **2018**, *10*, 44116−44125.

(21) Pappenfus, T. M.; Almyahi, F.; Cooling, N. A.; Culver, E. W.; Rasmussen, S. C.; Dastoor, P. C. Exploration of the Direct Arylation Polymerization Method for the Practical Application of Conjugated Materials: Synthetic Scale-Up, Solar Cell Performance, and Cost Analyses. *Macromol. Chem. Phys.* **2018**, *219*, 1800272.

(22) Hummelen, J. C.; Knight, B. W.; LePeq, F.; Wudl, F.; Yao, J.; Wilkins, C. L. Preparation and characterization of fulleroid and methanofullerene derivatives. *J. Org. Chem.* **1995**, *60*, 532−538.

(23) Holmes, N. P.; Marks, M.; Kumar, P.; Kroon, R.; Barr, M. G.; Nicolaidis, N.; Feron, K.; Pivrikas, A.; Fahy, A.; Mendaza, A. D. d. Z.; Kilcoyne, A. L. D.; Müller, C.; Zhou, X.; Andersson, M. R.; Dastoor, P. C.; Belcher, W. J. Nano-pathways: Bridging the divide between water-processable nanoparticulate and bulk heterojunction organic photovoltaics. *Nano Energy* **2016**, *19*, 495−510.

(24) Kilcoyne, A. L. D.; Tyliszczak, T.; Steele, W. F.; Fakra, S.; Hitchcock, P.; Franck, K.; Anderson, E.; Harteneck, B.; Rightor, E. G.; Mitchell, G. E.; Hitchcock, A. P.; Yang, L.; Warwick, T.; Ade, H. Interferometer-controlled scanning transmission X-ray microscopes at the Advanced Light Source. *J. Synchrotron Radiat.* **2003**, *10*, 125−136.

(25) Kosco, J.; Bidwell, M.; Cha, H.; Martin, T.; Howells, C. T.; Sachs, M.; Anjum, D. H.; Gonzalez Lopez, S.; Zou, L.; Wadsworth, A.; Zhang, W.; Zhang, L.; Tellam, J.; Sougrat, R.; Laquai, F.; DeLongchamp, D. M.; Durrant, J. R.; McCulloch, I. Enhanced photocatalytic hydrogen evolution from organic semiconductor heterojunction nanoparticles. *Nat. Mater.* **2020**, *19*, 559−565.

(26) Spano, F. C.; Clark, J.; Silva, C.; Friend, R. H. Determining exciton coherence from the photoluminescence spectral line shape in poly(3-hexylthiophene) thin films. *J. Chem. Phys.* **2009**, *130*, 074904.

(27) Schwarz, K. N.; Farley, S. B.; Smith, T. A.; Ghiggino, K. P. Charge generation and morphology in P3HT : PCBM nanoparticles prepared by mini-emulsion and reprecipitation methods. *Nanoscale* **2015**, *7*, 19899−19904.

(28) Ulum, S.; Holmes, N.; Darwis, D.; Burke, K.; David Kilcoyne, A. L.; Zhou, X.; Belcher, W.; Dastoor, P. Determining the structural motif of P3HT:PCBM nanoparticulate organic photovoltaic devices. *Sol. Energy Mater. Sol. Cells* **2013**, *110*, 43−48.

(29) Barr, M. G.; Chambon, S.; Fahy, A.; Jones, T. W.; Marcus, M. A.; Kilcoyne, A. L. D.; Dastoor, P. C.; Griffith, M. J.; Holmes, N. P. Nanomorphology of eco-friendly colloidal inks, relating non-fullerene acceptor surface energy to structure formation. *Mater. Chem. Front.* **2021**, *5*, 2218−2233.

(30) Vollath, D.; Fischer, F. D.; Holec, D. Surface energy of nanoparticles - influence of particle size and structure. *Beilstein J. Nanotechnol.* **2018**, *9*, 2265−2276.

(31) Tcholakova, S.; Mitrinova, Z.; Golemanov, K.; Denkov, N. D.; Vethamuthu, M.; Ananthapadmanabhan, K. P. Control of Ostwald ripening by using surfactants with high surface modulus. *Langmuir* **2011**, *27*, 14807−14819.

(32) Kabalnov, A. Ostwald ripening and related phenomena. *J. Dispersion Sci. Technol.* **2001**, *22*, 1−12.

(33) Xie, C.; Tang, X.; Berlinghof, M.; Langner, S.; Chen, S.; Späth, A.; Li, N.; Fink, R. H.; Unruh, T.; Brabec, C. J. Robot-Based High-Throughput Engineering of Alcoholic Polymer: Fullerene Nano-particle Inks for an Eco-Friendly Processing of Organic Solar Cells. *ACS Appl. Mater. Interfaces* **2018**, *10*, 23225−23234.